The role of turbulence stress divergence in decelerating a river plume

Levi F. Kilcher,[1] Jonathan D. Nash,[1] and James N. Moum[1]

Received 24 June 2011; revised 27 March 2012; accepted 2 April 2012; published 22 May 2012.

[1] Turbulence controls the composition of river plumes through mixing and alters the plume's trajectory by diffusing its momentum. While believed to play a crucial role in decelerating river-source waters, the turbulence stress in a near-field river plume has not previously been observationally quantified. In this study, finely resolved density, velocity, and turbulence observations are combined with a control-volume technique to describe the momentum balance in the Columbia River's near-field plume during 10 tidal cycles that encompass both large and small river flow. Turbulence stress varies by 2–3 orders of magnitude, both within a given ebb and between ebbs with different tidal or river forcing; its magnitude scales with the strength of the instantaneous ebb outflow, i.e., high stresses occur during peak flow of strong ebbs. During these periods, the momentum equation is represented by a balance between stress divergence and plume deceleration. As the flow relaxes, the stress divergence weakens and other terms (pressure gradient and Coriolis) may become appreciable and influence plume deceleration. While the momentum balance could not be closed during these weaker flow periods, during strong tidal pulses the time scale for decay based on observed stress is significantly less than a tidal half-period, indicating that stress divergence plays a fundamental role in the initial deceleration of the plume.

Citation: Kilcher, L. F., J. D. Nash, and J. N. Moum (2012), The role of turbulence stress divergence in decelerating a river plume, *J. Geophys. Res.*, *117*, C05032, doi:10.1029/2011JC007398.

1. Introduction

[2] Buoyant plumes form at the mouths of small and large rivers alike, dispersing freshwater, nutrients, toxins and organisms into coastal oceans around the world [*Halpern et al.*, 2008]. The impact and fate of these waters is controlled by their dilution (i.e., integrated mixing) and trajectory (i.e., changes in momentum).

[3] River plumes can be classified as dynamically small or large based on their horizontal length scale, L, compared to their Rossby radius, L_{Ro}. Large-scale plumes ($L > L_{Ro}$) are controlled by planetary rotation, wind and coastal currents [*Lentz*, 2004]. Small-scale plumes ($L < L_{Ro}$) are dominated by momentum advected from upstream, discharge geometry (e.g., spreading), and shear driven turbulence stress [*Garvine*, 1995].

[4] In large plumes exiting from narrow river mouths (less than L_{Ro}), a near-field region exists just outside the mouth which is dynamically similar to small-scale plumes [*Hetland*, 2005; *Horner-Devine et al.*, 2009]. In these cases, the river mouth acts as a hydraulic constriction which forces the estuary discharge to become super-critical (fluid speeds exceed the plume's internal wave speed) [*Armi and Farmer*, 1986]. As this fluid exits the river mouth it spreads and thins along the ocean surface, forming the near-field plume. Because flow speeds of these near-field plumes are generally larger than coastal flow speeds, they tend to dominate the dynamics near the mouth.

[5] Near-field plume dynamics have been known to be strongly influenced by turbulence stress, τ, and vertical mixing for some time [*Wright and Coleman*, 1971]. However, the relationships between the mean-flow properties that control this turbulence (e.g., shear, stratification, spreading) and the turbulence itself are complex and poorly understood. Lateral spreading, for example, enhances plume shear more rapidly than stratification, leading to enhanced susceptibility to shear-instability and turbulence [*Hetland*, 2010]. However, the resultant entrainment decelerates the plume, slows spreading and reduces shear. Thus, the ultimate structure of the plume depends on a delicate balance between spreading and mixing. Numerical models of plume evolution are thus sensitive to details of how turbulence is parameterized [*Garvine*, 1995; *Hetland*, 2010].

[6] Germane to discussion of these dynamics is the degree to which energy and momentum are lost across the plume base versus at the plume front, which tends to be highly dissipative but spans limited spatial extent [*Orton and Jay*, 2005; *Kilcher and Nash*, 2010]. For example, some studies have modeled plume structure assuming all dissipation occurs at the front [e.g., *Jay et al.*, 2010; *Garvine*, 1984].

[1]College of Oceanic and Atmospheric Sciences, Oregon State University, Corvallis, Oregon, USA.

Corresponding author: L. F. Kilcher, Department of Oceanic and Atmospheric Sciences, Oregon State University, 104 COAS Administration Bldg., Corvallis, OR 97331, USA. (lkilcher@coas.oregonstate.edu)

0148-0227/12/2011JC007398

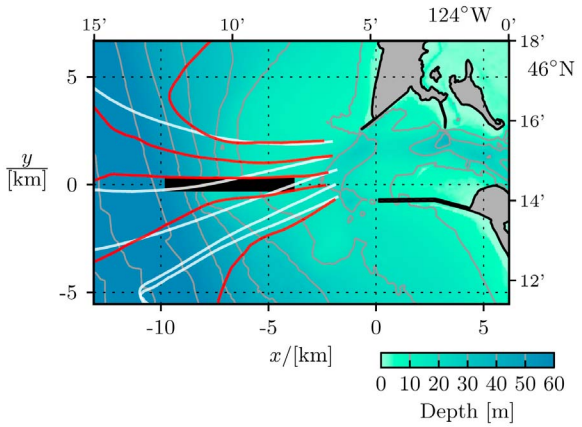

Figure 1. Bathymetry at the Columbia River mouth, with contours at 10 m intervals. The thick black line indicates the location of along-axis sampling. Shown for reference are paths of drifters released during the second ebbs of 9 and 19 August 2005 (red and white lines, respectively; data courtesy Ryan McCabe and Barbara Hickey).

Others, such as *Hetland* [2010], have focused on the dynamics at the plume base. In support of the latter, *McCabe et al.* [2009] found momentum advection to be balanced by $\partial\tau/\partial z$ within the plume base during peak ebb flow, with the caveat that the model did not have sufficient resolution to adequately represent dynamics at the plume front. Complicating this picture is the fact that the front can also lose energy through the radiation of nonlinear internal waves [*Nash and Moum*, 2005; *Pan and Jay*, 2007].

[7] Early measurements of turbulence in small-scale plumes investigated the influence of plume stratification on turbulence [*Luketina and Imberger*, 1989]. More recent efforts have focused on quantifying the influence of turbulence on plume dynamics and structure. Many of these studies have used "control volume" methods to estimate turbulence stress divergence and buoyancy flux [e.g., *MacDonald and Geyer*, 2004; *Chen and MacDonald*, 2006]. *MacDonald et al.* [2007] found reasonable agreement between such estimates and those based on shear probes mounted at the nose of an autonomous underwater vehicle. In our study of the Columbia River plume we make a similar comparison, in this case using τ estimates from vertical microstructure profiles.

[8] As in near-field plumes, estuary momentum balances indicate that $\partial\tau/\partial z$ is an important component of the dynamics [*Rippeth et al.*, 2002; *Kay and Jay*, 2003]. Furthermore, both of these domains are tidally forced, strongly sheared and stratified, and their turbulence is driven by shear instability [*Geyer and Smith*, 1987]. These similarities suggest that results applicable to shear-generated turbulence in estuaries have some applicability to that in near-field plumes, and vice versa. For example, it may be important to consider transport terms in the turbulence kinetic energy budget of near-field plumes, or to incorporate the gradient Richardson number dependence of the flux Richardson number when estimating turbulence fluxes [*Stacey et al.*, 1999; *Peters and Bokhorst*, 2001].

[9] However, a key difference between estuaries and near-field plumes is their geometry. Because plumes are not laterally constrained, spreading continually pushes the plume toward instability in a manner not present in the channel flow of a prototypical estuary. In addition, plumes are not subject to horizontal stirring by the estuary walls, but instead are influenced by coastal currents, winds and variable bathymetry.

[10] In the Columbia River near field, the strong ebb discharge through the mouth forms a rapidly expanding volume of buoyant fluid, bounded by a turbulent front as described by *Kilcher and Nash* [2010] (hereafter KN10). Initially, the front propagates slowly due to interaction with the shallow bathymetry near the mouth. After the water depth increases the front propagates as a gravity current at relatively constant speed until the ebb discharge weakens and the plume has expanded beyond L_{Ro}. At this time, the front decays, sometimes radiating nonlinear internal waves. Ultimately, the plume becomes part of the "bulge," or "re-circulating plume," described by *Horner-Devine* [2009].

[11] The primary objective of this work is to quantify the along-stream momentum balance of the near-field plume using observations of velocity, density and turbulence. In particular, we test the result from model simulations that $\partial\tau/lz$ can play an important role in fluid deceleration [*McCabe et al.*, 2009]. This analysis is based on observations of plume-base τ during ten tidal cycles of varying ebb strength and two periods of contrasting river flow.

[12] This paper is organized as follows. Sampling and data collection methods are described in section 2. In section 3, the evolution of ebb-discharge pulses is examined in terms of velocity, density and turbulence dissipation during periods of small and large river flow. In section 4, these data are combined to quantify the role of turbulence stress in the plume momentum budget. Conclusions and implications are presented in section 5. Details of the control-volume technique used in the analysis are included in Appendix A.

2. Setting and Data

[13] The Columbia River discharges into the Eastern Pacific Ocean between the states of Washington and Oregon (Figure 1). The bathymetry within 8 km of the river mouth is relatively flat, shallow (water depth, $d \approx 20$ m) and roughly radially symmetric around the tip of the north jetty. A 20 m deep dredged shipping channel, which runs from the river mouth to the southwest, is the primary exception to this symmetry. Offshore of 8 km the water depth increases rapidly from 20 to >60 m in only 2 km (Figure 1).

[14] The origin of our coordinate system is due north of the tip of the south jetty (46.24°N, 124.08°W) with the positive x, u and y, v directions eastward and northward respectively (Figure 1). The y-direction is roughly parallel to the north–south coastline. z is defined as positive upward from the ocean surface.

2.1. Sampling

[15] The evolution of the near-field plume throughout each tidal period was captured by sampling continuously while transiting along the plume axis. The "along-axis" transect is slightly south of the typical centroid of freshwater transport in the plume [see *Nash et al.* 2009], and approximately aligned with the mean river discharge, as indicated by drifter tracks in Figure 1. Transects were acquired at

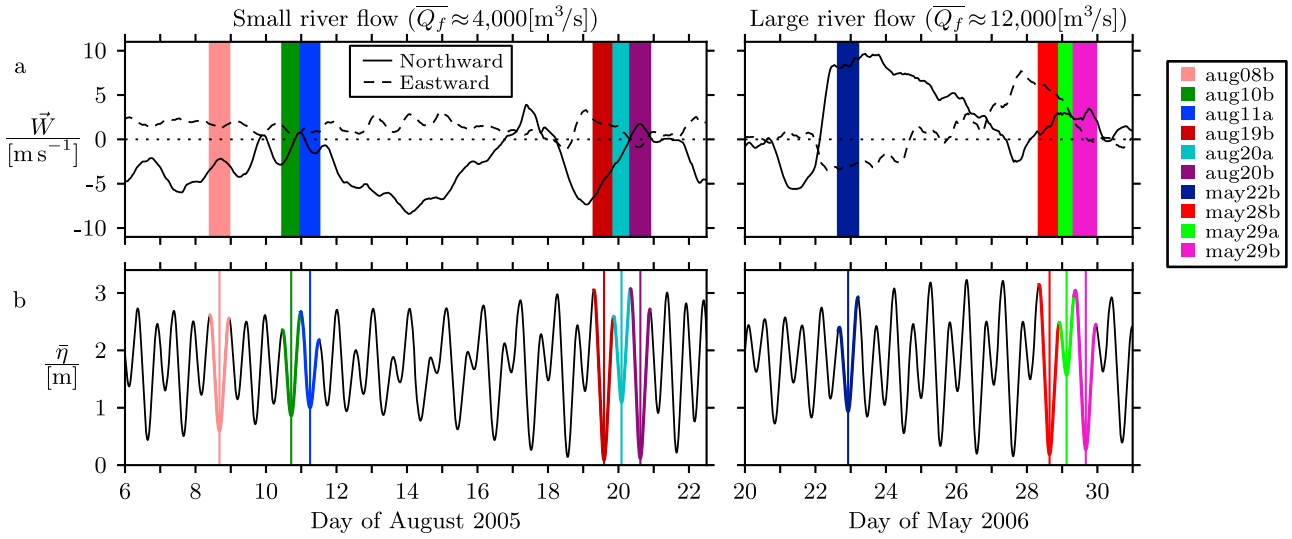

Figure 2. Environmental conditions at the Columbia River mouth during August 2005 and late May 2006: (a) 10 hour low-passed wind velocity from NDBC buoy 46029, Columbia River bar and (b) tidal height from XTide (see D. Flater, http://www.flaterco.com/xtide/, 2008). Periods of along-axis sampling are indicated in the legend at right. Days are marked at the start of the UTC day.

1–2 hour intervals while the ship made 2–3 m s^{-1} through the water (1–5 m s^{-1} over land).

[16] Data were obtained on 10- and 20-day field experiments in spring of 2006 and summer of 2005, respectively. The primary difference in environmental forcing between these periods was a change in daily-mean river flow, $\overline{Q_f}$. During August 2005, $\overline{Q_f} \approx 4000$ m^3 s^{-1} was near the mean annual cycle low. The May 2006 study took place during the spring freshet when the river flow was a factor of 3 larger, $\overline{Q_f} \approx 000$ m^3 s^{-1} [*Hickey et al.*, 2010].

[17] Six "along-axis" tidal periods were sampled in August 2005 and four in May 2006 (Figure 2). Tidal amplitudes had similar variability during these periods, often exhibiting large diurnal inequality. Each tidal period is assigned a "tidal ID," which is composed of a three-letter month prefix ('aug'/'may') followed by its numeric day of that month and an 'a' or 'b' to denote the first or second ebb of that day, respectively. These data resolve both spring and neap conditions (e.g., aug19b versus aug11a). All told, tidal amplitudes varied from $\Delta\bar{\eta} < 1$ m to ≈3 m, where $\Delta\bar{\eta} = \bar{\eta}_{high} - \bar{\eta}_{low}$ is the tidal elevation drop from the given ebbs preceding high tide ($\bar{\eta}_{high}$) to its low ($\bar{\eta}_{low}$). Tidal surface elevation, $\bar{\eta}$, is taken from "XTide" tidal height estimates at the "Columbia River N. Jetty" site (see D. Flater, http://www.flaterco.com/xtide/, 2008).

[18] Wind velocity, $\vec{W}$, from NDBC buoy 46029 (measured at 5 m above the surface and extrapolated to 10 m) is shown in Figure 2b. Winds were generally light to moderate ($|\vec{W}| < 8$ m s^{-1}) and upwelling favorable, except during 22–25 May 2006 when the winds were stronger ($|\vec{W}| \approx 11$ m s^{-1}) and downwelling favorable (Figure 2b).

2.2. Data

[19] This work combines shipboard acoustic Doppler current profiler (ADCP) and microstructure profiler measurements. Highly resolved profiles of salinity, s, temperature, T, and vertical shear of small-scale horizontal velocity, $\partial u'/\partial z$, were obtained from the Chameleon microstructure profiler using a fast-response thermistor, conductivity cell, and a pair of orthogonally mounted airfoil shear probes. With the aid of probe guards, Chameleon was routinely run into the seafloor, permitting measurements to within 2 cm of the bottom.

[20] To minimize contamination from the ship's wake, the profiler was loosely tethered from the ship's crane and deployed 5 m outboard of the starboard stern quarter. Buoyancy frequency, $N^2 = (-g/\rho_o)(\partial\rho_\theta/\partial z)$, is estimated from potential density, ρ_θ, profiles with background density $\rho_o = 1024$ kg m^{-3} and gravitational acceleration, $g = 9.81$ m s^{-2}. Plume freshwater fraction $j = (s_o - s)/s_o$ is defined using a background salinity of $s_o = 34.2$ psu. First-mode long-wave speeds, c, are computed numerically from N^2 profiles (no shear) [*Drazin and Reid*, 2004].

[21] Turbulence kinetic energy dissipation rate, ϵ, is estimated in 1-m bins from $\partial u'/\partial z$ spectra, corrected for lost variance at high wave numbers using theoretical spectra [*Moum et al.*, 1995]. The ϵ estimates are discarded where the profiler experienced excessive acceleration, vibration, or changes in orientation; the latter often affects data in the upper 4 m. Furthermore, contaminated ϵ data are identified as deep as 7 m depth when the ship's orientation and water column shear combined to place the profiler in the ship's wake. Because this form of contamination occurred preferentially when the ship was traveling westward, we have restricted the analysis to eastward transects. Further details can be found in *Nash et al.* [2009] and KN10.

[22] Horizontal velocity estimates ($u(z)$, $v(z)$) were obtained from a 1200 kHz ADCP mounted on a pole alongside the ship 1 m below the surface. This instrument measured water velocity in 0.5 m bins from 2.2 to 24.2 m depth. Because velocity profiles between the plume base and 2.2 m were quite straight, we use a linear fit to velocity data

between 2.2 and 4.7 m to extrapolate velocity data to the surface. Near the bottom, where ADCP estimates are invalid due to sidelobe interference with the bottom (below 85% of the water depth), velocity was linearly interpolated from the last valid bin to 0 at the bottom.

[23] High-frequency noise in ADCP-derived velocity has been reduced using a 3-bin by 5-bin (1.5 m vertically by 7.5 s in time) median filter. Eastward, $\partial u/\partial z$, and northward, $\partial v/\partial z$, shear are computed from these screened data and squared-shear computed,

$$S^2 = \left(\frac{\partial u}{\partial z}\right)^2 + \left(\frac{\partial v}{\partial z}\right)^2. \quad (1)$$

S^2 is further smoothed using a 1.5 m by 7.5 s Bartlett filter, producing a 10^{-3} s^{-2} noise floor. S^2 is not computed where u was extrapolated. Inverse gradient Richardson number, $Ri^{-1} = S^2 / N^2$, is computed when N^2 exceeds the S^2 noise floor. $Ri^{-1} > 4$ is the condition for shear instability in which the destabilizing effect of S^2 overwhelms the stabilizing influence of N^2.

[24] Vertical eddy viscosity, K_v, is estimated by assuming a constant flux Richardson number of $R_f = 0.17$ [*Moum*, 1990],

$$K_v = \frac{1}{1 - R_f}\frac{\epsilon}{S^2}. \quad (2)$$

Eddy viscosity estimates are combined with shear to estimate the x-z component of stress,

$$\tau = -K_v \frac{\partial u}{\partial z}. \quad (3)$$

[25] Bottom stress, τ_b, is estimated as $\tau_b = \langle \kappa z_b \epsilon \rangle_{ml}^{2/3}$, where $\kappa \approx 0.41$ is von Kármán's constant, z_b is the height above the bottom and $\langle\rangle_{ml}$ denotes an average over the bottom mixed layer [*Dewey and Crawford*, 1988]. Surface wind stress estimates, $\vec{\tau}_s$, are estimated using a quadratic drag law, $\vec{\tau}_s = \rho_{air} C_d \vec{W} |\vec{W}| / \rho_o$, where $\rho_{air} = 1.3$ kg m^{-3} is the density of air, and $C_d = 0.0012$ is the drag coefficient [*Large and Pond*, 1981].

2.3. Plume Definition and Other Notations

[26] The plume front location, x_f, is defined by the maximum horizontal velocity convergence at $z = -2.35$ m (identified only in transects in which the front appeared, KN10). Throughout this work, for each tidal period, time is relative to the time the front crossed the midpoint of the sampling region ($x = -7$ km). This is extrapolated from the actual time and location the front is identified assuming the front propagates at $U_f = 1$ m s^{-1} (KN10). The plume thickness, h_p, is defined as the depth where the velocity is one fourth its surface value:

$$h_p = -z(u(z) = u(0)/4). \quad (4)$$

While somewhat arbitrary, this definition can be effectively applied to continuously stratified and sheared plumes; more common definitions of plume depth based on an isopycnal or max N^2 were not effective because plume density changes as a function of time and stratification is often highest at the surface. Offshore of the front, $x < x_f$, h_p is undefined.

[27] The following notation is used to denote three averages: (1) $\langle\rangle$ denotes an average between $-9 < x < -5$ km; (2) $\langle\rangle_p$ denotes an average within the plume over the same range; and (3) $\langle\rangle_\epsilon$ is the same as $\langle\rangle_p$ but only includes regions where ϵ estimates are valid (i.e., below 3.5 m). Also, the notation $O()$ is used to denote the "order of magnitude" of a quantity.

3. Plume Structure and Evolution

[28] The evolution of two ebbs during small and large river flow ($\overline{Q_f} = 4,000$ and 12,000 m^3 s^{-1}) are shown in Figures 3 and 4, respectively. These ebbs both occurred during weak winds and their tidal amplitudes, $\Delta\bar{\eta} \approx 3$ m, were similar (Figure 2). Below, we describe the evolution of these ebbs in terms of five stages: pre-front, front, peak-ebb, mid-ebb and late-ebb. The vertical structure of these stages are shown in Figure 5 in terms of 1-km horizontal averages (except mid-ebb).

3.1. Pre-front

[29] During the pre-front stage, near-surface velocity and S^2 are weak compared to later stages (Figures 3b, 3d, 4b, 4d, 5b, and 5d). Buoyant fluid from a previous ebb is often present, elevating N^2 and lowering Ri^{-1} (Figures 3a, 3c, 3e, 4a, 4c, 4e, 5a, 5c, and 5e). The near-surface turbulence is typically low, $\epsilon < O(10^{-6}$ W kg$^{-1})$ at $z = -4$ m (f).

3.2. Front

[30] The frontal region is characterized by strong surface velocity convergence (magenta bar in "front" column, subjectively identified based on isopycnal displacement and velocity structure). The internal structure of the plume front is markedly different during large- versus small- $\overline{Q_f}$. Plume fluid inshore of the frontal region is more dense (less buoyant) during small $\overline{Q_f}$ than large. This allows surface convergence to produce strong vertical displacements, turbulence and bottom interactions during small $\overline{Q_f}$ (Figure 3). The increased buoyancy of plume fluid during large-$\overline{Q_f}$ apparently limits vertical displacement at the front, resulting in weakened turbulence and no bottom interactions (Figure 4). *Spahn et al.* [2009] showed that the strong bottom interactions observed during small-$\overline{Q_f}$ produce bursts of resuspended sediment that detach from the bottom and are swept offshore.

3.3. Peak Ebb

[31] At peak-ebb, surface fluid flows offshore at >2 m s^{-1} and S^2 is high (Figures 3 and 4b, 4d). During large $\overline{Q_f}$ plume density and thickness are significantly lower than during small $\overline{Q_f}$ (Figure 4a),resulting in higher N^2, stronger S^2, and higher surface fluid speeds (Figures 4b, 4c, and 4d). *Nash et al.* [2009] suggest these differences are related to changes in the ratio between advective (horizontal) and turbulent (vertical) buoyancy fluxes in the estuary, which scales with $\overline{Q_f}$. Within the plume, Ri^{-1} was similarly supercritical for both ebbs; it was >10 in some places ($Ri = .1$).

[32] The near-linear velocity profile and bands of S^2 which reach toward the bottom during the front and peak-ebb stages of small $\overline{Q_f}$ suggest this flow interacts with the

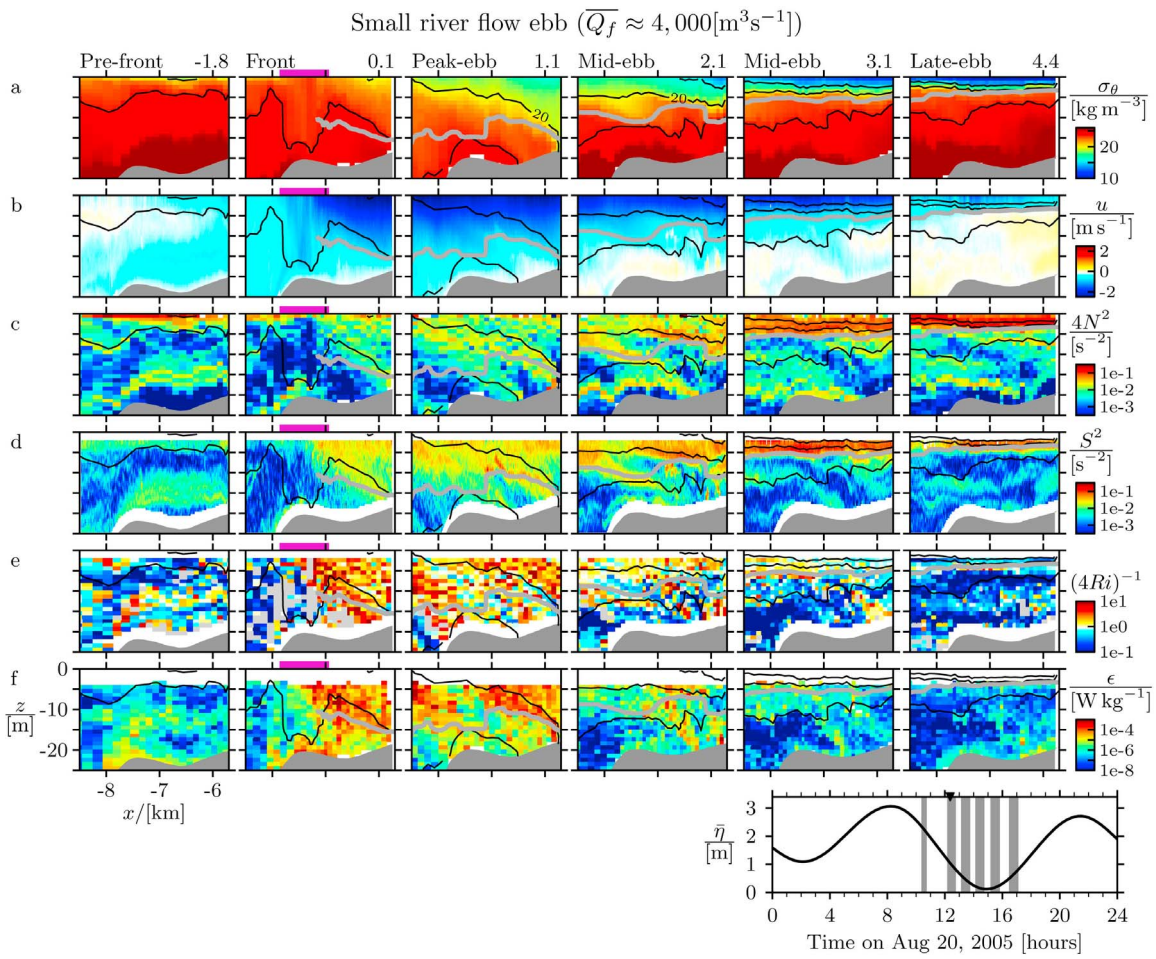

Figure 3. A time series of spatial snapshots during the small $\overline{Q_f}$ ebb aug20b (2005). Plots shown are (a) σ_θ, (b) u, (c) 4 N^2, (d) S^2, (e) 4 Ri^{-1}, and (f) ϵ. Black lines are σ_θ = 16, 20, and 24 kg m^{-3} contours, and thick gray lines indicate h_p. The magenta bar and black triangle above plots in the "front" column mark the "frontal region" and x_f, respectively. Regions of undefined Ri^{-1} are indicated in gray. All transects were acquired traveling eastward with mean time in hours shown above Figure 3a; all are relative to the time the ship crossed $x = -7$ km, indicated as a black triangle in the plot at bottom right, which shows the tidal elevation at the N Jetty and times of sampling (gray).

bottom; during large $\overline{Q_f}$ the plume's velocity structure is confined to the upper 8 m (Figure 5b). During large $\overline{Q_f}$, the plume is thinner and faster, thus producing higher S^2, N^2 and ϵ (compare red profiles in the top versus bottom plots of Figures 5b, 5c, 5d, and 5f). The strongest ϵ occurs where both S^2 and Ri^{-1} are high.

3.4. Mid-Ebb

[33] Throughout mid-ebb the plume thins and surface fluid speed and density both decrease, combining to produce a slight increase in plume N^2 and S^2. These changes happen proportionally, so that Ri^{-1} remains super-critical. Where ϵ is resolved (near and just above the plume base, i.e., gray line) it is reduced from that observed during peak-ebb, but still elevated well above pre-front levels ($>O(10^{-5}$ W kg^{-1})). During small $\overline{Q_f}$, bands of elevated Ri^{-1} and ϵ below the plume suggest that bottom interaction can persist until this stage.

3.5. Late Ebb

[34] The trends of decreasing plume thickness, surface density and fluid speeds continue into late-ebb. In contrast to mid-ebb, this occurs such that plume S^2 drops more rapidly than 4 N^2, Ri^{-1} becomes sub-critical, and ϵ decreases. While the highest ϵ may occur above the region we measured, the decrease in Ri^{-1} is consistent with weakening ϵ. Onshore flow below the plume ($z < -h_p$) during this phase indicates a reversal in tidal flow and movement of the salt wedge upstream.

3.6. Plume Evolution: Summary

[35] Five stages of the tidal plume structure have been presented in the previous sections. Here, the time evolution is quantified in terms of spatial averages of j, u, Ri, ϵ, etc., for both small and large $\overline{Q_f}$ (Figure 6). Data represent averages over the near field (−9 to −5 km) and above $z = -h_p$ (see section 2.3 for details). Exceptions are the pre-front ($t < 0$) and front ($t = 0$) averages, which are computed over the

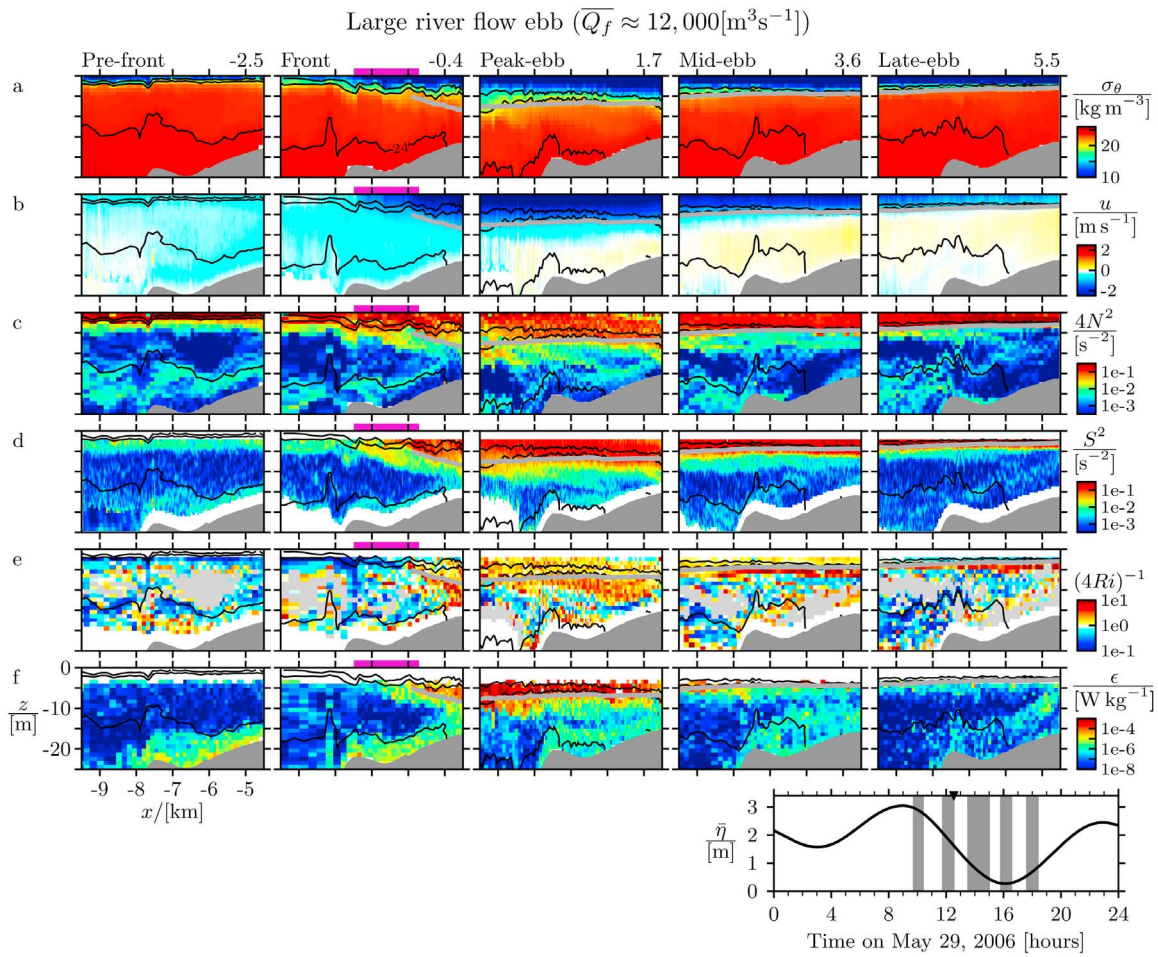

Figure 4. Time series of spatial snapshots through the large $\overline{Q_f}$ ebb may29b (2006). Transects are approximately 2 hours apart. All plots and annotations are the same as in Figure 3.

initial plume thickness, but horizontally restricted to fluid either offshore or inshore of the front. Quantities are not particularly sensitive to the details of this averaging.

[36] Most quantities exhibit dramatic changes as the front passes. For both small and large $\overline{Q_f}$, plume velocity increases sharply, as does S^2, Ri^{-1} and ϵ (Figures 6c–6f). However there are significant differences between the two data sets. For example, during large $\overline{Q_f}$ the plume is initially thinner and fresher than during small $\overline{Q_f}$ (Figures 6a and 6b), producing higher N^2 (Figure 6d, dashed lines). During both large and small $\overline{Q_f}$, high plume velocities drive S^2 to exceed 4 N^2, causing super-critical Ri^{-1} and powering intense turbulence (Figures 6d–6f). It is noteworthy that j and N^2 increase less dramatically across the front during small $\overline{Q_f}$; i.e., the density front is not as "sharp" during weaker stratification, although it is more dramatic in terms of vertical displacements.

[37] For the first four hours after frontal passage, the plumes thin and j increases while u remains relatively constant. Thus, S^2 and N^2 both increase, resulting in a gradual decrease in Ri^{-1} (but still super-critical). Not including the front, turbulent dissipation and internal stress is highest during peak-ebb (Figures 6f and 6g). During late ebb, u decreases so that S^2 is less than 4 N^2 and Ri^{-1} insufficient for instability.

[38] Looking at each ebb individually, the highest values of $\langle Ri^{-1} \rangle_p$ are associated with the largest values of $\langle \epsilon \rangle_\epsilon$. However, comparing these quantities between ebbs reveals a contrasting story. The largest $\langle Ri^{-1} \rangle_p$ occurs during small $\overline{Q_f}$ conditions (aug20b), while the largest $\langle \epsilon \rangle_\epsilon$ occurs during large $\overline{Q_f}$ (may29b). This suggests that a parameterization for ϵ based on energy available for dissipation, e.g. $S^2 - 4\,N^2$, may perform better than one based on Ri^{-1} or S^2 alone [*Kunze et al.*, 1990].

4. Plume Momentum

[39] Our goal is to determine the role of turbulence stress divergence in the momentum balance of the near-field Columbia River plume. This work focuses on the dynamics at the plume base, where horizontal gradients of density and velocity are much smaller than at the front (KN10). Applying the Boussinesq approximation and assuming divergences of turbulence fluxes are larger in the vertical than the horizontal, the along-axis momentum equation is

$$\frac{\partial u}{\partial t} + \vec{u} \cdot \vec{\nabla} u - fv + \frac{\partial P}{\partial x} + \frac{\partial \tau}{\partial z} = 0. \qquad (5)$$

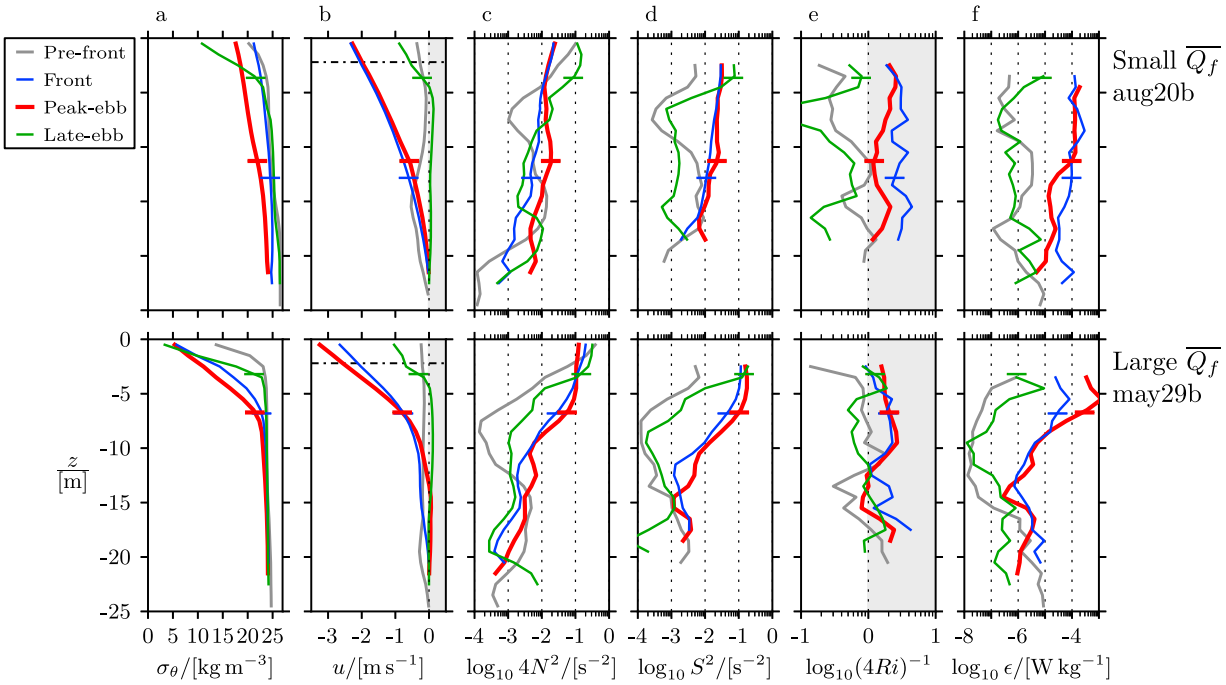

Figure 5. Average profiles during example (top) small $\overline{Q_f}$ (aug20b) and (bottom) large $\overline{Q_f}$ (may29b) ebbs. The profiles are taken as the average over the range $-7 < x < -6$ km, except for the "front" profiles, in which the average is over the 1 km inshore of the frontal region. Shown left to right are (a) u, (b) σ_θ, (c) 4 N^2, (d) S^2, (e) $(4Ri)^{-1}$, and (f) ϵ. Horizontal ticks across the "Peak-ebb" and "Late-ebb" profiles indicate h_p. In Figure 5a, the shaded region indicates onshore velocities, and the dash-dot line indicates the depth above which velocity was extrapolated. In Figure 5e, the shaded region indicates $Ri < 1/4$.

Here, P is the reduced pressure, which can be written in terms of its baroclinic (P_bc) and barotropic (P_η) components assuming a hydrostatic balance:

$$P = \underbrace{\frac{g}{\rho_\circ}\int_z^0 \rho \mathrm{d}z'}_{} + \underbrace{g\eta}_{} = P_\mathrm{bc} + P_\eta, \tag{6}$$

where $\rho_\mathrm{o} = 1024.6$ kg m^{-3} is the reference density and η is the surface displacement.

[40] Our observations directly resolve most of the terms in equation (5), which are detailed in Figure 7. The local acceleration, $\partial u/\partial t$, is computed from the observed change in velocity between consecutive transects. The Coriolis acceleration, $-fv$, is computed directly from the observed northward velocity. The baroclinic pressure gradient, $\partial P_\mathrm{bc}/\partial x$, is estimated from the observed density field. The stress profile is estimated from the measured shear and ϵ according to equation (3).

[41] The advective term, $\vec{u}\cdot\vec{\nabla}u$, consists of three parts, $u\frac{\partial u}{\partial x} + v\frac{\partial u}{\partial y} + w\frac{\partial u}{\partial z}$. The first of these is measured directly, the second is assumed to be zero along a plume streamline (i.e., the plume axis), and the third is determined using a control-volume method similar to that of *MacDonald and Geyer* [2004] (hereafter MG04). This involves estimating lateral spreading (the rate at which non-dimensional plume width, $b(x)$, increases with $-x$; i.e., db / dx), by conserving freshwater flux along the transect. As detailed in Appendix A, db/dx is used in a volume conservation equation to obtain an estimate of w, allowing $w\frac{\partial u}{\partial z}$ to be estimated.

[42] Uncertainty in this term is dominated by error in db/dx, likely associated with short-time-scale variability in the freshwater flux. This uncertainty is quantified by estimating $w\frac{\partial u}{\partial z}$ using values of db/dx equal to the freshwater conservation estimate (which typically ranged from .06 to 0.16 km^{-1}) plus or minus 0.06 km^{-1}. Uncertainty is also introduced through the assumption of $v\frac{\partial u}{\partial y} = 0$ (see section A4).

[43] The remaining term in equation (5), the surface pressure gradient, $\partial P_\eta/\partial x$, is also not measured directly. We estimate it so that it balances the depth-integrated form of equation (5), with observed τ_s and τ_b used as upper and lower boundary conditions, respectively (see section A3).

[44] Throughout this section, data are presented with respect to a scaled depth coordinate,

$$z^* = \frac{z}{h_\mathrm{p}(x)}. \tag{7}$$

Because our focus is the plume and its base ($z^* = -1$), we henceforth limit our attention to the depth range $0 > z^* > -1.6$. All terms are evaluated within a control volume that extends from $x = -5$ to -9 km.

[45] In the following we first investigate the momentum balance of a single, example transect which highlights the importance of τ. We then examine an average formed from a subset of transects which individually close equation (5).

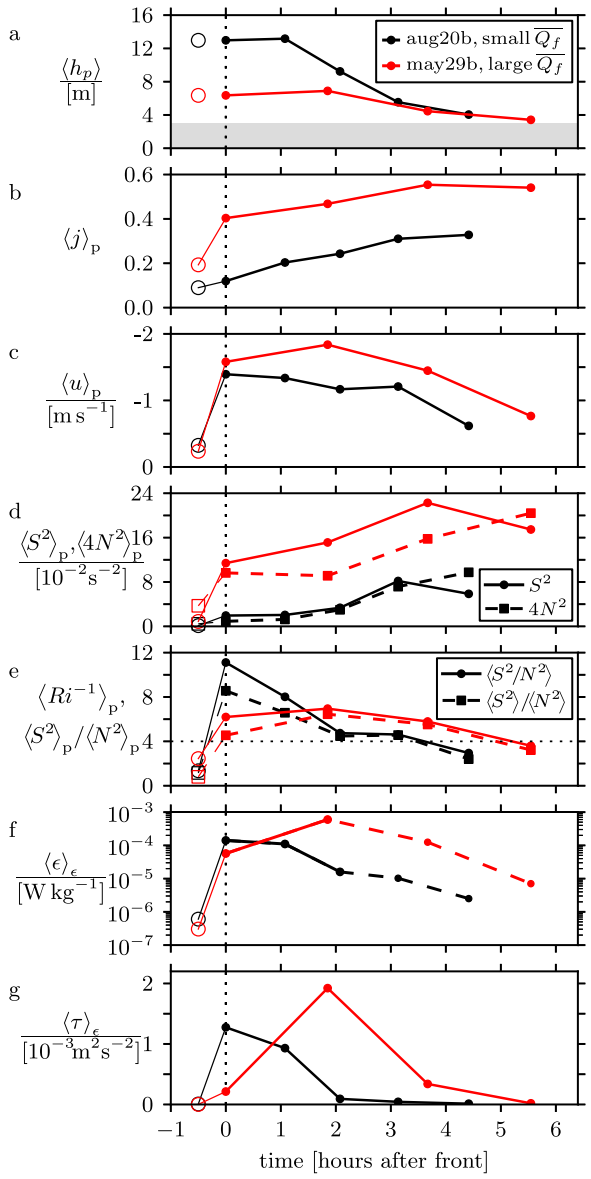

Figure 6. Plume-averaged quantities versus time of ebbs aug20b (black) and may29b (red): (a) plume thickness, h_p, (b) freshwater fraction, $\langle j \rangle_\mathrm{p}$, (c) $\langle u \rangle_\mathrm{p}$, (d) $\langle S^2 \rangle_\mathrm{p}$ and $\langle 4N^2 \rangle_\mathrm{p}$, (e) $\langle Ri^{-1} \rangle_\mathrm{p}$ and $\langle S^2 \rangle_\mathrm{p} / \langle N^2 \rangle_\mathrm{p}$, (f) $\langle n \rangle_\epsilon$, and (g) $\langle \tau \rangle_\epsilon$. Open symbols in Figures 6b–6g are the average of each quantity offshore of the front, over the initial plume thickness (open circle in Figure 6a). The shaded region in Figure 6a indicates the region where profiler tilt was too high to estimate ϵ. In Figure 6f the line is dashed where ϵ estimates were made in less than 40% of the plume.

This is followed by an examination of a complimentary subset, in which the balance is not closed.

4.1. Example Momentum Balance: A Greater Ebb During Small $\overline{Q_f}$ (August 2005)

[46] Here we examine each term in the momentum balance for the peak ebb of aug20b, a greater ebb during small $\overline{Q_f}$ and weak upwelling winds (Figure 3). This transect was acquired one hour after frontal passage. The plume was thick (h_p = 11 m), isopycnal slopes high, and flow offshore throughout the water column with shear increasing toward the surface (Figure 8a).

4.1.1. Acceleration

[47] At peak ebb, the local acceleration is positive throughout the water column, $\partial u/\partial t > 0$, indicating that offshore flow speeds decrease with time (Figure 8b, magenta). $\partial u/\partial t$ is largely barotropic, suggesting that it is associated with time dependence of the barotropic tide, and not specifically deceleration of the plume, which is surface-intensified. The $u\frac{\partial u}{\partial x}$ term is positive throughout the plume, indicating a convergence of offshore momentum (Figure 8b, solid blue). Below the plume, this term is zero.

[48] The dark blue dashed line indicates the value of the $w\frac{\partial u}{\partial z}$ term using the freshwater conservation estimate of spreading (db/dx = 0.16 km^{-1}). This term is zero at the surface for all spreading estimates because w is defined to be zero there. Below that, this term is negative (w is positive and du/dz is negative), indicating a divergence of offshore momentum which roughly cancels the convergence from the $u\frac{\partial u}{\partial x}$ term in the middle of the plume. Shading in Figure 8b represents the range in $w\frac{\partial u}{\partial z}$ when different spreading rates are assumed (db/dx = 0.1 and 0.22 km^{-1} in this case.)

[49] The total acceleration, $\frac{Du}{Dt} = \frac{\partial u}{\partial t} + u\frac{\partial u}{\partial x} + w\frac{\partial u}{\partial z}$, is positive at the surface, indicating that offshore moving fluid parcels are slowing down (Figure 8c, purple). Because we are concerned with offshore-flowing parcels, throughout the remainder of this work we refer to positive Du/Dt as "deceleration." Within the lower three-quarters of the plume ($-0.25 > z^* > -1$), deceleration is weaker, and not statistically different from zero. Below the plume, parcels are not accelerating. While there is significant uncertainty in Du/Dt within and below the plume, its value near the surface is better constrained because it does not depend on spreading assumptions.

4.1.2. Coriolis Acceleration

[50] Upwelling favorable winds during August 2005 produced a weak southward flow along the Washington coast,

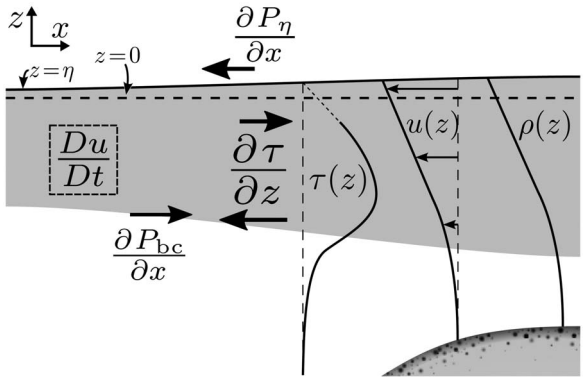

Figure 7. Diagram of plume and terms in the plume momentum equation. The gray shaded region represents light plume fluid flowing to the left. The speckle-shaded region marks the bottom. Schematic profiles of turbulence stress, velocity, and density are on the right. Forces are indicated by line arrows. Imbalance in the forces will cause acceleration. The Coriolis effect is not indicated in the schematic.

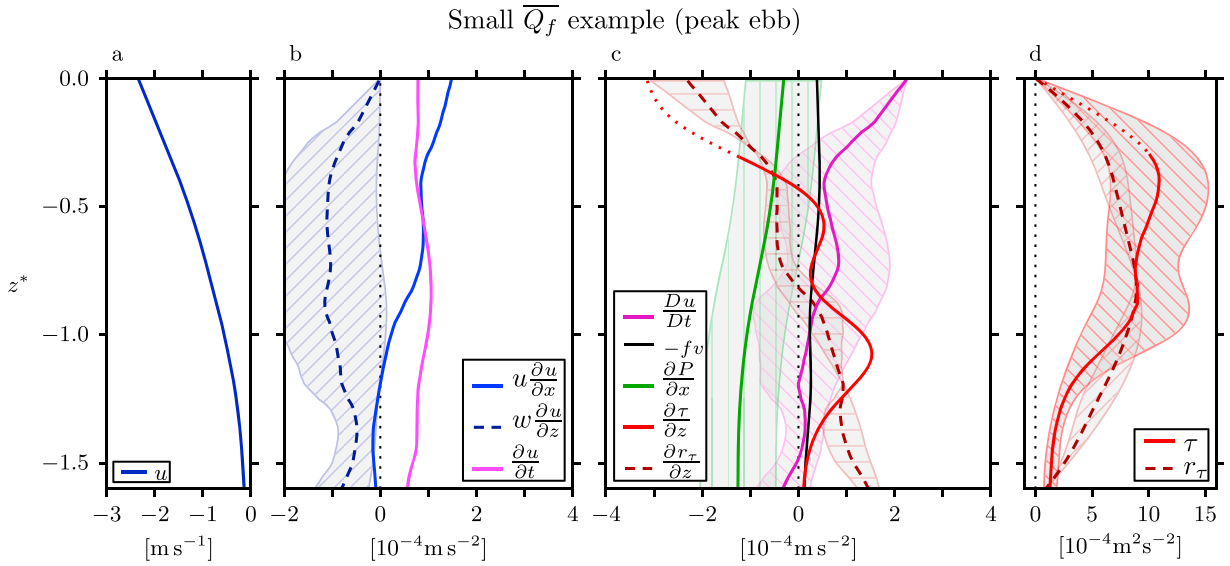

Figure 8. Terms in the u momentum equation during peak ebb of aug20b (Figure 3), versus scaled depth (h_p = 11 m). Each profile is an average across the transect (−9 km < x < −5 km). (a) Horizontal velocity, u. (b) Components of the total cross-shore acceleration. (c) Terms in the cross-shore momentum balance. (d) Internal stress, τ, and control-volume residual-stress, r_τ. Shaded regions in Figures 8b and 8c and for r_τ (in Figure 8d) indicate uncertainty related to plume spreading. Shading around τ (in Figure 8d) is the 95% bootstrap confidence interval of the profiles in the transect. In Figures 8c and 8d, the dotted red line indicates the region where τ is interpolated between τ_s and the nearest-surface value. The τ and $\partial\tau/\partial z$ profiles were smoothed with a 2.5 m half-width triangle filter.

resulting in a contribution from the Coriolis term (Figure 8). This term is smaller but the same sign as Du/Dt, suggesting that it too requires a shoreward force to balance it. The finding that fv is relatively small is consistent with *McCabe et al.*'s [2009] model results of the Columbia River plume during August 2005.

4.1.3. Pressure Gradient

[51] The surface pressure gradient, estimated as a residual in the depth-integrated balance with τ_s and τ_b used as boundary conditions, is near zero (Figure 8c, green at $z^* = 0$). Therefore, it does not force the large deceleration of surface fluid. Error bounds on the surface pressure gradient term are propagated from the error in the $w\frac{\partial u}{\partial z}$ term associated with different assumed spreading rates.

[52] In this example, the baroclinic pressure gradient (the vertical structure of green curve, ∂P_{bc} / ∂x), is non-negligible. Its maximum magnitude is about half that of the near-surface material deceleration. However, while the total pressure gradient acts to decelerate offshore-flowing fluid, the sign of $\partial P_{bc}/\partial x$ has the effect of increasing $\partial\tau/\partial z$ required to balance the observed Du/Dt, albeit weakly. This is the largest baroclinic pressure gradient we observed (note the steep isopycnal shoaling in Figure 3c), suggesting that, in general, $\partial P_{bc}/\partial x$ is not a dominant term in the plume-base momentum balance.

4.1.4. Internal Stress

[53] The internal stress, τ, exceeds 10^{-3} m^2 s^{-2} within the plume and decreases with depth (Figure 8d, red). Positive stress indicates downward flux of offshore momentum. In contrast, the surface wind stress ($\tau_s \approx 3 \times 10^{-6}$m^2 s^{-2}) and bottom stress ($\tau_b < O(10^{-4}$m^2 s^{-2})) are each much smaller and do not apply a dynamically significant force on the plume. Within the plume τ is several orders of magnitude higher than τ_s, implying a large near-surface stress divergence (Figures 8c and 8d red dotted line). Note that there is a factor of 2 uncertainty in τ associated with sampling of lognormally distributed turbulence (Figure 8d [*Moum et al.*, 1995]).

[54] In this example, the magnitude and sign of near-surface stress divergence is approximately equal and opposite to Du/Dt (compare purple and red in Figure 8c), suggesting that $\partial\tau/\partial z$ controls the observed deceleration in the upper plume. Within the middle third of the plume, τ is relatively constant, which agrees with the weak deceleration there. At the plume base, τ decreased rapidly, thereby transmitting momentum lost near the surface into fluid at the plume base. Near-surface momentum is thus transported by turbulence through the plume and deposited near $z^* = -1$. While the control-volume technique indicates a corresponding deceleration of near-surface fluid, it does not indicate an acceleration of fluid (Du/Dt) at $z^* = -1$ consistent with the observed stress divergence there. While $\partial P_{bc}/\partial x$ balances some of $\partial\tau/\partial z$, it does not have sufficient vertical structure to balance all of it.

4.1.5. Residual Stress

[55] Without direct estimates of internal stress divergence, MG04 estimated it as a residual in the momentum budget,

$$\frac{\partial r_\tau}{\partial z} = -\frac{Du}{Dt} - \frac{\partial P}{\partial x} + fv \tag{8}$$

We refer to this as the "residual-stress" divergence (Figure 8c, dashed dark-red line). It represents the force

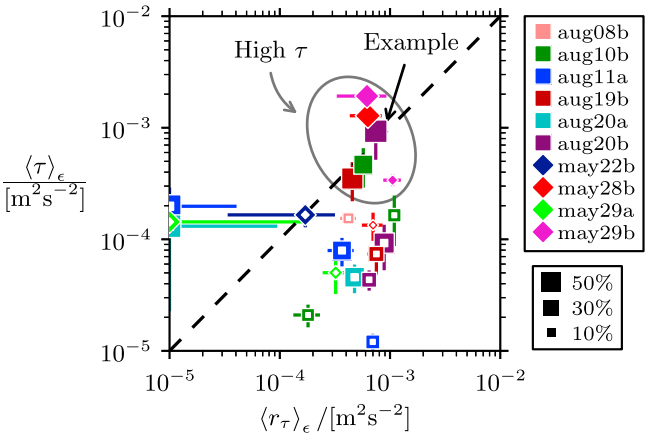

Figure 9. Average turbulence stress, $\langle\tau\rangle_\epsilon$, versus control-volume residual stress, $\langle r_\tau\rangle_\epsilon$. Each point is from a single transect during an ebb (top legend). Error bars on r_τ represent the uncertainty associated with spreading assumptions, while the error bars on τ indicate the 95% confidence interval of measured stresses. Marker area is proportional to the fraction of the plume in which ϵ was resolved (bottom legend). The $\langle\tau\rangle_\epsilon$ estimates greater than 3×10^{-4} m^2 s^{-2} are circled; lower values have a white center. Three data points on the left edge of the plot have negative $\langle r_\tau\rangle_\epsilon$. A black arrow marks the point corresponding to the "example" transect of section 4.1.

required to balance the control-volume's estimate of acceleration after accounting for the pressure gradient and Coriolis effect. This is independent of the surface pressure gradient estimate because that term was estimated using the observed τ_s and τ_b at the upper and lower boundaries. Therefore, according to equation (8), τ_s and $r_\tau = \tau_s, \tau_b$ at the surface and bottom, respectively. Note that error in r_τ is smaller than that of Du/Dt and $\partial P/\partial x$ because the error associated with spreading assumptions cancels as the individual terms are summed. However, we also note that error associated with the assumption that $\nu\frac{\partial u}{\partial y} = 0$ is not included here.

[56] Comparison of $\partial r_\tau/\partial z$ with $\partial\tau/\partial z$ is an alternate way to assess the accuracy of the control-volume method. In particular, agreement of the magnitude of $\partial r_\tau/\partial z$ with $\partial\tau/\partial z$ suggests that, in this example, the control-volume method produces a reasonable estimate of plume deceleration.

[57] At the plume base, however, $\partial r_\tau/\partial z$ does not agree with $\partial\tau/\partial z$. This is the same discrepancy as that between plume acceleration and $\partial\tau/\partial z$ near $z^* = -1$. Here, it is manifested as $\partial r_\tau / \partial z$ being roughly constant below $z^* = -1$, rather than showing a peak near $z^* = -1$ (as observed in $\partial\tau/\partial z$). This results in a gradually changing r_τ below $z^* = -1.3$ (Figure 8d). Interpreting r_τ as an estimate of stress would suggest that there is a stress divergence well below the plume base (i.e., to the bottom), when in fact we observe none.

4.1.6. Summary of Example Balance

[58] In summary, during peak ebb and small $\overline{Q_f}$ (Figure 3c), the dominant dynamic balance in the upper plume is between deceleration and internal stress divergence (Figure 8c). The $\partial\tau/\partial z$ profile indicates that turbulence transports momentum from the near-surface waters downward through the plume and deposits it at the plume base ($z^* = -1$). The baroclinic pressure gradient plays a lesser role in the momentum balance, acting to weakly accelerate surface-plume waters relative to those below. All other terms in equation (5) (surface pressure gradient, Coriolis acceleration, surface and bottom stresses) are relatively small.

4.2. Assessing Control-Volume Accuracy: All Ebbs

[59] To assess the general applicability of the control-volume method, we diagnose all terms in the momentum balance for each ebb transect of the 10 tidal cycles sampled (Figure 2). As a means of evaluating whether the near-surface deceleration is captured by the measured stress divergence in the upper plume, we compare $\langle r_\tau\rangle_\epsilon$ to $\langle\tau\rangle_\epsilon$ (Figure 9); recall that $\langle\rangle_\epsilon$ indicates an average over the plume but restricted to the region where turbulence data are available.

[60] The comparison is not particularly good: While $\langle\tau\rangle_\epsilon$ varies by more than 2 orders of magnitude, $\langle r_\tau\rangle_\epsilon$ has very little dynamic range. The majority of $\langle r_\tau\rangle_\epsilon$ estimates are $\approx 10^{-3}$ m^2 s^{-2}, and a few are even negative, which is nonphysical and indicates error in our control-volume assumptions. Errors associated with uncertainty in plume spreading accounts for this discrepancy in a few cases (horizontal error bars), but not in the majority of them.

[61] There are two possible sources for this discrepancy: (1) Our turbulence observations have failed to capture the region of peak stress, and/or (2) the control-volume technique has poor fidelity due to invalidity of the assumption that $\nu\frac{\partial u}{\partial y} = 0$. Estimates of this term from transects across the plume axis, during different ebbs than investigated here, reveals that its variability has sufficient magnitude to account for the discrepancy between r_τ and τ (see section A4). This suggests that future studies may need to accurately resolve this term, simultaneously to making along-axis measurements, in order to estimate r_τ.

4.3. Mean Momentum Balance

[62] We now seek to quantify the momentum balance of the Columbia River near-field plume in an averaged sense. Based on Figure 9 we divide the data into two sets: (1) a "high stress" set in which $\langle r_\tau\rangle_\epsilon$ and $\langle\tau\rangle_\epsilon$ are similar and hence the momentum balance closes, and (2) a "low-stress" set in which the magnitude of $\langle r_\tau\rangle_\epsilon$ is generally much larger than $\langle\tau\rangle_\epsilon$. Note that the latter include cases in which $\langle r_\tau\rangle_\epsilon$ is negative and hence cannot be balanced by a traditional down-gradient momentum flux.

4.3.1. High Stress/Peak Ebb

[63] Figure 10 shows averaged profiles of velocity, acceleration, momentum and stress from the high-τ transects (circled in Figure 9), which are generally associated with the initial stages of each ebb pulse (i.e., peak-ebb in Figures 3 and 4). The structure of the terms in the momentum balance for high-τ transects is similar to the example in Figure 8. Local deceleration, $\partial u/\partial t$, is positive throughout the water column, and largely barotropic on average (Figure 10b, magenta). Within the upper half of the plume ($z^* > -0.5$) $u\frac{\partial u}{\partial x}$ is positive and dominates the acceleration terms (Figure 10b, solid blue). Below the plume $u\frac{\partial u}{\partial x}$ is nearly zero and $w\frac{\partial u}{\partial z}$ roughly balances $\partial u/\partial t$. This results in a total acceleration profile that indicates parcels decelerate strongly

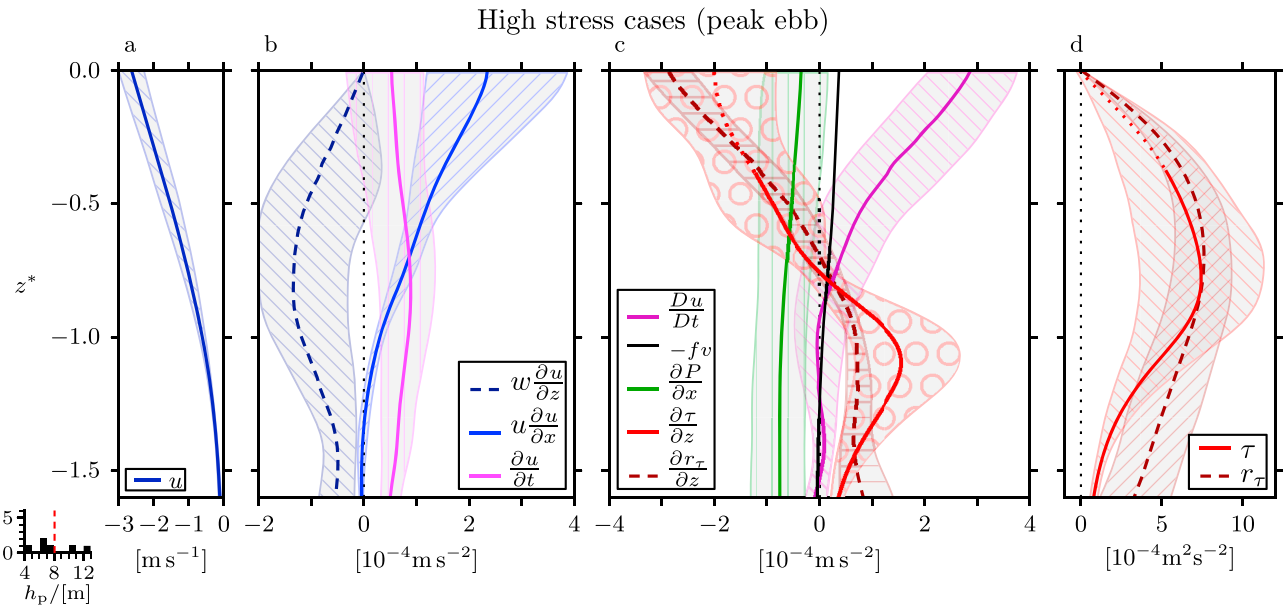

Figure 10. Terms in the u momentum balance, ensemble averaged over high-τ transects, versus scaled depth. Each line represents the mean of the profiles (lines in Figure 8), averaged over the six high-τ transects. The shading about each line indicates the 95% boot-strap confidence interval of those profiles. The plots are as in Figure 8. A histogram of plume thicknesses in this ensemble average is at bottom left; the dashed-red line indicates the average.

near the surface, yet negligibly at and below h_p (Figure 10c, purple). Despite significant transect-to-transect variability in the constituent terms (i.e., Figure 10b), Du/Dt is well constrained both within the plume and below.

[64] Compared to Du/Dt, $-fv$ and $\partial P_{BC}/\partial x$ are weak. The $\partial P_{BC}/\partial x$ term is small because this analysis focuses on the weakly sloping plume base, and does not include the front–where the baroclinic pressure gradient drives frontal propagation. $\partial P\eta/\partial x$ and $\partial u/\partial t$ are roughly in balance ($\approx$0.5 m s^{-2}) and predominantly tidal. The surface and bottom stresses are small compared to internal τ (Figure 10d, red). Overlap of the 95% confidence intervals of r_τ and τ suggests consistency between the control-volume derived deceleration and the observed τ.

[65] $\partial\tau/\partial z$ is the dominant force in the balance (Figure 10c, red): internal stresses flux momentum from the upper two-thirds of the plume downward, where it is deposited at the plume base. As in the aug20b example (section 4.1), the control-volume method does not capture this input of momentum implied by the observed stress divergence at $z^* = -1$ (Figure 10c, purple).

4.3.2. Low Stress/Later Ebb

[66] In the remainder of the ebb transects, resolved τ was up to a factor of 10 smaller than the high-τ cases and significantly less than (or of opposite sign to) r_τ required to close the momentum balance. These transects generally corresponded to weak ebbs (small $\Delta\bar{\eta}$) and/or mid- to late-stages of the ebb flow. The mean vertical structure of momentum terms are shown in Figure 11.

[67] The mean velocity has a similar shape but is 25% weaker than that of the high-τ cases (compare Figure 11a to Figure 10a). As a result, $u\frac{\partial u}{\partial x}$ is almost 50% weaker than in the high-τ cases. However, the time dependence in the low-τ cases ($\partial u/\partial t \approx 0.8 \times 10^{-4}$ m s^{-2}), is larger than in the high-τ cases (compare magenta lines in Figures 10b and Figure 11b). As in the high-u case, $\partial u/\partial t$ is mostly barotropic and associated with the surface tide, which changes more-rapidly during mid and late ebb. The control-volume estimate of the pressure gradient encourages this interpretation; $\partial P_\eta/\partial x$ is similar magnitude to the depth-average of $\partial u/\partial t$. The fact that $\partial P/\partial x$ shows little vertical structure indicates that $\partial P_{BC}/\partial x$ is negligible in the low-τ cases (i.e., isopycnals are horizontal during mid- and late-ebb so internal pressure gradients are weak). The Coriolis term is also small compared to Du/Dt but of similar magnitude to $\partial P_\eta/\partial x$ and $\partial\tau/\partial z$.

[68] In contrast to the high-τ balance (Figure 10), in these low-τ cases, the resolved $\partial\tau/\partial z$ is too small to balance near-surface Du/Dt. This results in a mismatch between $\partial\tau/\partial z$ and $\partial r_\tau/\partial z$ (Figure 11c, red versus dark-red dashed). As mentioned in section 4.2, this imbalance could be attributed to: (1) errors in control-volume estimates of Du/Dt resulting from the $v\frac{\partial u}{\partial y} = 0$ assumption, and/or (2) because the plumes in Figure 11 were often thinner than those in Figure 10 it is possible we have failed to measure the strongest ϵ in these cases, so that the maximum stress and divergence are underestimated. While this second possibility is a concern for low-stress cases involving thin plumes, some low-stress cases involved plumes with $h_p > 8$ m. In these cases we resolved τ in >%50 of the plume (large markers in Figure 9), and error in control-volume estimates of Du/Dt is the most likely source of discrepancy between $\partial r_\tau/\partial z$ and $\partial\tau/\partial z$.

4.4. Plume Deceleration

[69] We now seek to determine the importance of turbulence stress in the context of the scales imposed by the

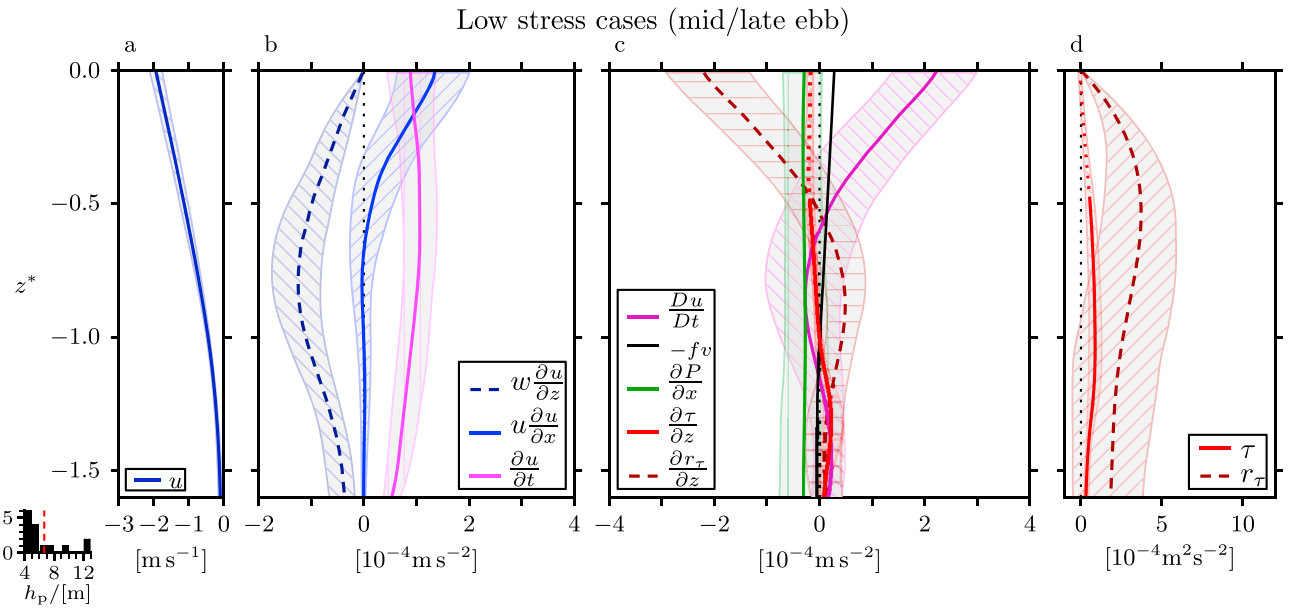

Figure 11. Terms in the u momentum balance, averaged over the 15 low-τ transects, versus scaled depth. All plots are as in Figure 10.

geometry, time dependence (i.e., tidal forcing) and upstream conditions (i.e., river flow) of the system. We frame this discussion in terms of time scales. The outer time scales are the tidal and Coriolis half-periods, 6 and 8 h respectively. Assuming the plume decelerates as a slab, the time scale for turbulent decay can be estimated as $T_\tau = \langle h_p \rangle \langle u \rangle_p / \langle \tau \rangle_\epsilon$.

[70] At the beginning of each strong ebb pulse, T_τ is small (less than 6 h), suggesting that τ is sufficient to decelerate the plume before it either adjusts to the Earth's rotation or runs out of fluid from the current ebb pulse (Figure 12; KN10). As the ebb progresses (mid- and late-ebb), the plume thins, slows down, and resolved τ weakens, so that T_τ increases (Figure 12). Thus, as the ebb relaxes, turbulence within the near field becomes less important in the momentum balance, consistent with the results presented in section 4.3.2. During low-τ ebbs and the later period of all ebbs, either the plume adjusts through rotation and pressure gradients, or the internal stresses become more important farther offshore, where the plume thins and may have a strongly dissipative front (i.e., KN10).

4.5. External Forcing

[71] Why do some ebbs emerge with high τ, and others with low τ? Based on the anecdotal evidence presented in Figures 5 and 6, S^2 appears to be a controlling parameter in setting ϵ and τ. Since S^2 scales with the tidally driven plume velocity, we anticipate τ to depend on the tidal amplitude at the river mouth, $\Delta\bar{\eta}$, which has significant variability (Figure 2b). In order to collapse data from the small- and large-$\overline{Q_f}$ seasons, τ is normalized by the square of the internal wave speed c^2, which increases with $\overline{Q_f}$ and accounts for the seasonal changes in N^2 and h_p. Figure 13 shows that peak-ebb τ/c^2 is strongly dependent on tidal amplitude: All large ebbs ($\Delta\bar{\eta} \approx 3$ m) initially emerge with high τ.

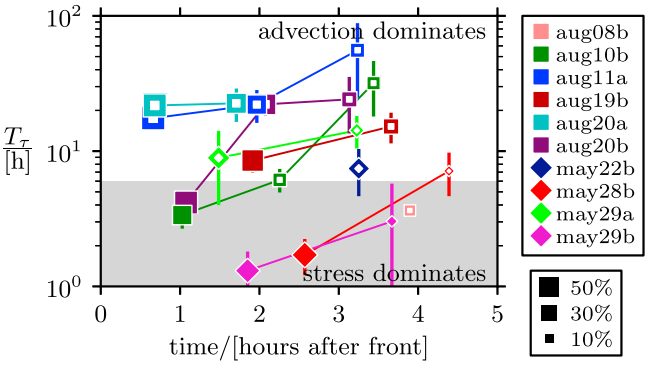

Figure 12. Deceleration time scale T_τ as a function of time since frontal passing. Markers are as in Figure 9; line segments join data from transects during a single ebb. Shading indicates times less than a tidal half period. Error bars are 95% confidence intervals.

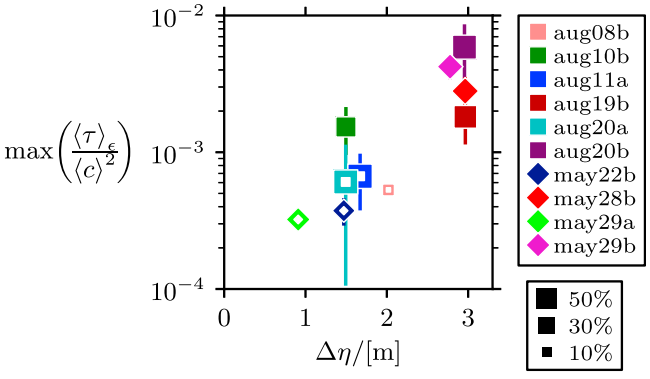

Figure 13. Transect-averaged stress at peak ebb versus tidal amplitude. Markers are as in Figure 9. Error bars are 95% confidence intervals.

[72] On longer time scales, seasonal changes in $\overline{Q_f}$ and spring-neap variability in estuary mixing control the composition and vertical structure of the near-field plume [*Nash et al.*, 2009]. Through the associated changes in c^2, these upstream processes thus influence the magnitude of τ for a given $\Delta\bar{\eta}$. However, for each tidal cycle, $\Delta\bar{\eta}$ controls the instantaneous Ri and S^2, and thus sets the scale for τ and its importance for the plume's initial deceleration. Within each ebb τ/c^2 decays with time (i.e., Figure 12), an attribute that accounts for at least some of the data scatter in Figure 13, since each "peak-ebb" was sampled at a differenttime within the tidal cycle.

5. Conclusions

[73] The tidal evolution of the Columbia River's near-field plume has been investigated using turbulence observations that span a range of tidal amplitudes and freshwater river input. Our observations capture the plume's evolution, beginning with the passage of a highly turbulent front that bounds each ebb pulse, through a period of strong ebb discharge that slowly decreases in strength, to its ultimate decay to a more passive plume at late ebb.

[74] During small river flow (August 2005, $\overline{Q_f} \approx 4000$ m^3 s^{-1}), large tidal discharge velocities in the presence of modest stratification forced strong S^2, $Ri < 1/4$, and high ϵ throughout much of the water column. During large river flow (May 2006, $\overline{Q_f} \approx 12{,}000$ m^3 s^{-1}), the plume was thinner and fresher, supporting higher S^2 and ϵ. Data from both field seasons were used to diagnose terms in the along-stream momentum budget using direct turbulence observations combined with a control-volume method similar to MG04.

[75] Despite the marked ebb-to-ebb and seasonal differences in vertical structure, a unified picture of the near-field evolution exists. As the plume emerges, it tends to be thick, highly sheared and intensely turbulent; τ plays an important role in decelerating plumes released during moderate to strong ebb pulses, as characterized by the tidal amplitude, $\Delta\bar{\eta}$. As time evolves, the plume thins, resulting in higher S^2 but reduced Ri^{-1}. As a consequence, resolved ϵ and τ decrease in time.

[76] We have divided our data into two sets, each distinguished by the magnitude of the measured internal stress at the plume base. These are termed either high or low τ. Ebb-to-ebb variability between these two extremes is characterized by the strength of each ebb pulse: the maximum normalized stress τ/c^2 is found to strongly scale with $\Delta\bar{\eta}$. Within a given ebb, the dynamics progress from high to low τ.

[77] We have resolved, in detail, the plume momentum balance when τ is high. At peak ebb, $\partial\tau/\partial z$ controls plume deceleration. That is, $\partial\tau/\partial z$ balances Du/Dt within the plume; all other terms ($\partial P/\partial x$, fv, τ_b and τ_s) are weak by comparison (Figure 10). Momentum supplied near the surface from upstream is transported downward by turbulence and deposited at the plume base. In these cases $T_\tau < 6$ h indicates that turbulence decelerates the plume before the estuary forcing subsides or the flow becomes geostrophically adjusted [KN10; *Garvine* 1995]. This suggests that inviscid models of plume expansion [e.g., *Garvine*, 1984; *Jay et al.*, 2010; KN10] might be improved by incorporating frictional effects.

[78] Dominant terms in the near-field momentum balance differ from those farther upstream in the Columbia River estuary [*Kay and Jay*, 2003]. In the estuary, $\partial\tau/\partial z$, Du/Dt and $\partial P/\partial x$ each play a role in the super-tidal momentum balance. In contrast, internal pressure gradients appear to play a weaker role within the near-field plume (away from the front), because isopycnals tend to be close to horizontal. Additionally, surface pressure gradients should also be weak since they must be balanced by $\partial P_{BC}/\partial x$ in order for near-bottom accelerations to be small. This finding, that pressure gradients are small, is likely a general attribute of all plumes that are disconnected from the bottom.

[79] During the weaker flows that occur during neap tides, lesser ebbs, or late in the ebb pulse, resolved τ is a factor of 10 less than during high-τ periods. During these low-τ periods, we are unable to close the momentum balance ($r_\tau \neq \tau$). Either our measurements did not capture the region of highest τ, or unresolved lateral fluxes caused the control-volume technique to over-estimate plume deceleration (or implied negative momentum diffusivities). At these times, $T_\tau > 6$ h based on resolved τ suggests that the near-field plume can be considered largely inviscid (Figure 12).

[80] Under both low- and high-τ conditions the surface stress was near zero. While this implies large $\partial\tau/\partial z$ near the surface due to the large interior τ, it also suggests that winds did not impart significant momentum to the plume near field, even during periods of low internal τ. During periods of stronger winds than observed here ($\geq$15 m s^{-1}), it is possible that τ_s could play a role in the plume's momentum balance, especially in the cross-stream direction not considered here. Furthermore, winds have an increasingly important role farther offshore where the plume is thinner, wider and less directly influenced by the discharge from the river mouth.

[81] The high-τ cases, in which the plume momentum balance closes, represent the first direct confirmation of MG04's control-volume technique. However, at the plume base, the strong and localized $\partial\tau/\partial z$ we observed is not replicated by the control volume method, which instead suggests the stress should be transmitted into the lower water column where $\partial r_\tau/\partial z$ is distributed over a broad range of depths.

[82] Under the weaker, low-τ, conditions the control-volume estimate of deceleration is almost an order of magnitude larger than the other measured terms. As a result, the residual $\partial\, r_\tau/\partial\, z$ far exceeds the observed $\partial\tau/\partial z$. Moreover, r_τ has very little dynamic range (from ebb to ebb), while measured τ varies by several orders of magnitude, suggesting the control volume technique has poor fidelity or our measurements did not capture the near-surface stress maximum. Hence, caution is warranted in the interpretation of results based solely on the control-volume method. Error in the control-volume technique arises from a combination of (1) error in our estimates of lateral spreading, (2) time-dependence and high-frequency variability that is not included in the control-volume method, and (3) invalidity of the $v\frac{\partial u}{\partial y} = 0$ assumption (see section A4 for further details).

[83] In summary, the turbulence stress, τ, is found to vary by 2–3 orders of magnitude within each tidal cycle, in

between ebbs, and in response to seasonal changes in forcing. Specifically:

[84] 1. $\partial\tau/\partial z$ drives plume deceleration during the beginning of moderate-to-large ebb pulses. At these times, the plume's turbulence decay scale, T_τ, is short compared to the tidal or Coriolis half-period (6–8 h), and stresses inferred from MG04's control-volume technique are consistent with those directly observed.

[85] 2. As the tidal pulse decays, $\partial\tau/\partial z$ weakens and we are unable to close the momentum balance; T_τ increases.

[86] 3. The normalized stress, τ/c^2, scales with tidal amplitude, $\Delta\bar{\eta}$.

[87] Together, these results provide a systematic understanding of the role of turbulence stress in decelerating a tidally dominated near-field plume.

Appendix A: Control Volume (Accounting for Lateral Spreading)

[88] As indicated in the text, the primary purpose of the control-volume method is to obtain an estimate of w that is consistent with a realistic estimate of the plume's spreading, so that the $\vec{u}\cdot\vec{\nabla}u = u\frac{\partial u}{\partial x} + w\frac{\partial u}{\partial z}$ term in equation (5) can be estimated. In order to assume that $v\frac{\partial u}{\partial y}$ is zero, data inputs must be along the plume's trajectory (the plume axis). The validity of this assumption is discussed in section A4.

[89] The surface pressure gradient depends on the control-volume method because it is estimated as a remainder of terms that include $\vec{u}\cdot\vec{\nabla}u$. In this appendix we detail the steps for estimating w and $\partial P_\eta/lx$, as well as provide details of how other terms (that do not include spreading) are calculated within the context of the control-volume method.

[90] The control-volume method is a box model in which lateral (i.e., y-direction) fluxes are constrained using a plume width b, which is a function of x. The plume width is defined as the cross-plume distance between the lateral bounding surfaces of the plume, across which fluxes of momentum, salt and mass are defined to be zero. We have written b nondimensionally as, $b = R^{-1}(x - x_o)B(z) + 1$, where $x_\circ = -7$ km is the center of the sampling domain, R is a length parameter (i.e., a spreading radius) determined by conserving freshwater, and $B(z)$ is $O(1)$ and sets the depth dependence of the spreading. Following MG04, different forms for $B(z)$ were tested (constant with depth, linearly decreasing with depth, exponential decrease with depth, etc.), and it was found that terms in equation (5) were relatively insensitive to the form of $B(z)$. In contrast, terms in equation (5) change substantially with changes in R. Hence, we assume $B = 1$ for all of our analyses and quantify error in the control-volume method in terms of uncertainty in R.

[91] The control-volume method involves integrating the freshwater and volume conservation equations in two directions: (1) the y-direction from $-b(x)/2$ to $b(x)/2$, and (2) in the z direction from the ocean surface down to an arbitrary lower surface. Here we use the scaled depth surfaces, z^* = Constant, as the lower boundary of the control volume. In order to approximate a flow snapshot, data for a given transect were interpolated to the median time of each transect using the previous, current and subsequent transects as required.

A1. Plume Spreading

[92] The plume width, $b(x)$, is estimated using the control-volume freshwater conservation equation,

$$\int_{-d}^{0} jbu\,dz = Q_f. \tag{A1}$$

The integral is evaluated at the x-location of each microstructure profile. Assuming Q_f does not depend on x, $b(x)$ can be estimated as the best fit line that satisfies (equation A1). For the example transect of section 4.1, this method yields $R \approx 6$ km for aug20b's spreading parameter. This agrees with the spreading estimate from drifter releases during ebb aug19b (24 h earlier) of $R \approx 6.7$ km (white lines in Figure 1).

[93] The form of (equation A1) weights the spreading estimate heavily in the plume, where j and u are large. This provides a reasonable estimate for spreading within the plume, but is a poor representation of lateral fluxes below the plume base. This is the primary reason the control-volume method does not apply much below $z^* \approx -1$ (a more detailed consideration of this issue is given in MG04's Appendix B).

A2. Vertical Velocity

[94] Assuming that b does not vary in time, the volume conservation equation is,

$$w(z^*) = \frac{1}{b}\left\langle \frac{\partial}{\partial x}\int_{h_{pz^*}}^{0} bu\,dz \right\rangle. \tag{A2}$$

This gives an estimate of the quasi-vertical velocity normal to z^* surfaces. Throughout this work, averages of x-gradients of a quantity $G(x)$, (i.e., $\left\langle \frac{\partial}{\partial x}G \right\rangle$) are estimated as theslope of the linear best fit to $G(x)$. This has the advantage of including all data in a transect in the estimate of the gradient (rather than an average of a finite difference, which is merely a difference of the endpoints).

[95] With this estimate of w, $\vec{u}\cdot\vec{\nabla}u$ becomes,

$$\vec{u}\cdot\vec{\nabla}u = u\frac{\partial u}{\partial x} + w\frac{\partial u}{\partial z} = \frac{1}{2}\left\langle \frac{\partial u^2}{\partial x} \right\rangle + w\left\langle \frac{\partial u}{\partial z} \right\rangle. \tag{A3}$$

A3. Surface Pressure Gradient

[96] The surface pressure gradient, $\partial P_\eta/\partial x$, is estimated so that the depth-integrated momentum equation balances (with observed τ_s and τ_b applied as boundary conditions). The error in this term, therefore, includes the accumulated bias in all other terms. This includes error in $\vec{u}\cdot\vec{\nabla}u$ due to the $v\frac{\partial u}{\partial y} = 0$ assumption, and uncertainty in spreading.

A4. Control-Volume Residual

[97] The control-volume estimate of stress, r_τ, is computed as a residual of the other terms in equation (5) and thus accumulates error associated with natural variability in the flow, as well as any questionable assumptions. Based on the above analyses, the assumptions of the form of the plume's

spreading (that enter the $w\frac{\partial u}{\partial z}$ term), do not account for the discrepancy between r_τ and τ (Figure 9). Assuming that error in r_τ due to high-frequency variability of the outflow is small, this leaves two possible sources of error for this discrepancy: (1) our sampling did not resolve τ within the plume, and (2) the assumption that $v\frac{\partial u}{\partial y}$ is small is inaccurate.

[98] The first is a possible source of error for plumes that were undersampled because of small thickness. However, many of the low-τ plumes were sampled as completely as the high-τ cases, suggesting that this does not account for the mismatch in Figure 9, and that error is associated with $v\frac{\partial u}{\partial y} = 0$.

[99] The assumption $v\frac{\partial u}{\partial y} = 0$ can be satisfied if the sampling transect is aligned with a plume streamline (i.e., $v = 0$), and/or the plume is symmetric about that transect, so that $du/dy = 0$. Indeed, the non-zero magnitude of the Coriolis term in Figures 8, 10, and 11 indicates a $|v|$ as large as ≈0.3 m/s. Because our transect was aligned with the x-axis, this $v \neq 0$ indicates that sampling is not precisely along a streamline (e.g., white drifter tracks in Figure 1).

[100] From transects across the plume axis during different ebbs than presented here, we found $\frac{\partial u}{\partial y}$ has a near-zero mean but a standard deviation of 6×10^{-4} s^{-1}. Combined with $|v| \approx 0.3$ m/s, this gives an error in the control-volume estimate of $\vec{u} \cdot \vec{\nabla} u$, and $\partial r_\tau/\partial z$ of $\pm 2 \times 10^{-4}$ m s^{-2}. This is sufficient to account for the discrepancy between r_τ and τ in the low-stress cases, and suggests that future studies may need to accurately characterize these terms to make reasonable estimates of the residual, r_τ.

[101] **Acknowledgments.** The OSU Ocean Mixing group provided invaluable support in preparation for cruises, and during data collection. In particular, we thank A. Perlin, R. Kreth, and M. Neeley-Brown for their technical expertise. Special thanks to Dan MacDonald and two anonymous reviewers for helpful comments on earlier versions of this manuscript. The authors thank R. M. McCabe and B. M. Hickey for sharing surface drifter data used in Figure 1. Many thanks to S. Kelly, R. Bjorkquist, D. Franklin, E. Spahn, G.Avicola, A. Horner-Devine, and the captain and crew of the R/V *Pt. Sur* for making data collection possible. Funding for this research was provided by NSF grant OCE-0238727.

References

Armi, L., and D. M. Farmer (1986), Maximal two-layer exchange through a contraction with barotropic net flow, *J. Fluid Mech.*, *164*, 27–51.

Chen, F., and D. G. MacDonald (2006), Role of mixing in the structure and evolution of a buoyant discharge plume, *J. Geophys. Res.*, *111*, C11002, doi:10.1029/2006JC003563.

Dewey, R. K., and W. R. Crawford (1988), Bottom stress estimates from vertical dissipation rate profiles on the continental shelf, *J. Phys. Oceanogr.*, *18*, 1167–1177.

Drazin, P. G., and W. H. Reid (2004), *Hydrodynamic Stability*, 2nd ed., Cambridge Univ. Press, New York.

Garvine, R. W. (1984), Radial spreading of buoyant, surface plumes in coastal waters, *J. Geophys. Res.*, *89*, 1989–1996.

Garvine, R. W. (1995), A dynamical system for classifying buoyant coastal discharges, *J. Phys. Oceanogr.*, *15*, 1585–1596.

Geyer, W. R., and J. D. Smith (1987), Shear instability in a highly stratified estuary, *J. Phys. Oceanogr.*, *17*, 1668–1679.

Halpern, B. S., et al. (2008), A global map of human impact on marine ecosystems, *Science*, *319*, 948–952.

Hetland, R. D. (2005), Relating river plume structure to vertical mixing, *J. Phys. Oceanogr.*, *35*, 1667–1688, doi:10.1175/JPO2774.1.

Hetland, R. D. (2010), The effects of mixing and spreading on density in near-field river plumes, *Dyn. Atmos. Oceans*, *49*(1), 37–53, doi:10.1016/j.dynatmoce.2008.11.003.

Hickey, B. M., et al. (2010), River influences on shelf ecosystems: Introduction and synthesis, *J. Geophys. Res.*, *115*, C00B17, doi:10.1029/2009JC005452.

Horner-Devine, A. (2009), The bulge circulation in the Columbia River plume, *Cont. Shelf Res.*, *29*, 234–251, doi:10.1016/j.csr.2007.12.012.

Horner-Devine, A., D. A. Jay, P. M. Orton, and E. Y. Spahn (2009), A conceptual model of the strongly tidal Columbia River plume, *J. Mar. Syst.*, *78*, 460–475, doi:10.1016/j.jmarsys.2008.11.025.

Jay, D. A., E. D. Zaron, and J. Pan (2010), Initial expansion of the Columbia River tidal plume: Theory and remote sensing observations, *J. Geophys. Res.*, *115*, C00B15, doi:10.1029/2008JC004996.

Kay, D. J., and D. A. Jay (2003), Interfacial mixing in a highly stratified estuary: 2. A "method of constrained differences" approach for the determination of the momentum and mass balances and the energy of mixing, *J. Geophys. Res.*, *108*(C3), 3073, doi:10.1029/2000JC000253.

Kilcher, L. F., and J. D. Nash (2010), Structure and dynamics of the Columbia River tidal plume front, *J. Geophys. Res.*, *115*, C05S90, doi:10.1029/2009JC006066.

Kunze, E., A. J. I. Williams, and M. G. Briscoe (1990), Observations of shear and vertical stability from a neutrally buoyant float, *J. Geophys. Res.*, *95*(C10), 18,127–18,142.

Large, W. G., and S. Pond (1981), Open ocean momentum flux measurements in moderate to strong winds, *J. Phys. Oceanogr.*, *11*, 324–336.

Lentz, S. (2004), The response of buoyant coastal plumes to upwelling-favorable winds, *J. Phys. Oceanogr.*, *34*, 2458–2469, doi:10.1175/JPO2647.1.

Luketina, D. A., and J. Imberger (1989), Turbulence and entrainment in a buoyant surface plume, *J. Geophys. Res.*, *94*, 12,619–12,636.

MacDonald, D. G., and W. R. Geyer (2004), Turbulent energy production and entrainment at a highly stratified estuarine front, *J. Geophys. Res.*, *109*, C05004, doi:10.1029/2003JC002094.

MacDonald, D. G., L. Goodman, and R. D. Hetland (2007), Turbulent dissipation in a near-field river plume: A comparison of control volume and microstructure observations with a numerical model, *J. Geophys. Res.*, *112*, C07026, doi:10.1029/2006JC004075.

McCabe, R. M., P. MacCready, and B. M. Hickey (2009), Ebb tide dynamics and spreading of a large river plume, *J. Phys. Oceanogr.*, *39*, 2839–2856, doi:10.1175/2009JPO4061.1.

Moum, J. N. (1990), The quest for K_p—Preliminary results from direct measurements of turbulent fluxes in the ocean, *J. Phys. Oceanogr.*, *20*(12), 1980–1984.

Moum, J. N., M. Gregg, R. C. Lien, and M. E. Carr (1995), Comparison of turbulence kinetic energy dissipation rate estimates from two ocean microstrucure profilers, *J. Atmos. Oceanic Technol.*, *12*(2), 346–366.

Nash, J. D., and J. N. Moum (2005), River plumes as a source of large-amplitude internal waves in the coastal ocean, *Nature*, *437*, 400–403, doi:10.1038/nature03936.

Nash, J. D., L. F. Kilcher, and J. N. Moum (2009), Structure and composition of a strongly stratified, tidally pulsed river plume, *J. Geophys. Res.*, *114*, C00B12, doi:10.1029/2008JC005036.

Orton, P. M., and D. A. Jay (2005), Observations at the tidal plume front of a high-volume river outflow, *Geophys. Res. Lett.*, *32*, L11605, doi:10.1029/2005GL022372.

Pan, J., and D. A. Jay (2007), Analyses of internal solitary waves generated at the Columbia River plume front using SAR imagery, *J. Geophys. Res.*, *112*, C07014, doi:10.1029/2006JC003688.

Peters, H., and R. Bokhorst (2001), Microstructure observations of turbulent mixing in a partially mixed estuary: II. Salt flux and stress, *J. Phys. Oceanogr.*, *31*, 1105–1119.

Rippeth, T. P., E. Williams, and J. H. Simpson (2002), Reynolds stress and turbulent energy production in a tidal channel, *J. Phys. Oceanogr.*, *32*, 1242–1251, doi:10.1175/1520-0485(2002)032<1242:RSATEP>2.0.CO;2.

Spahn, E. Y., A. R. Horner-Devine, J. D. Nash, and L. F. Kilcher (2009), Particle re-suspension in the Columbia River plume near-field, *J. Geophys. Res.*, *114*, C00B14, doi:10.1029/2008JC004986.

Stacey, M. T., S. G. Monismith, and J. R. Burau (1999), Observations of turbulence in a partially stratified estuary, *J. Phys. Oceanogr.*, *29*, 1950–1970.

Wright, L. D., and J. M. Coleman (1971), Effluent expansion and interfacial mixing in the presence of a salt wedge, Mississippi River delta, *J. Geophys. Res.*, *76*(36), 8649–8661.